



# Probing myeloid cell dynamics in ischaemic heart disease by nanotracer hot-spot imaging

Max L. Senders<sup>1,2</sup>, Anu E. Meerwaldt<sup>1,3</sup>, Mandy M. T. van Leent<sup>1,2</sup>, Brenda L. Sanchez-Gaytan<sup>1,4</sup>, Jan C. van de Voort<sup>1</sup>, Yohana C. Toner<sup>1</sup>, Alexander Maier<sup>1</sup>, Emma D. Klein<sup>1</sup>, Nathaniel A. T. Sullivan<sup>1</sup>, Alexandros Marios Sofias<sup>1,5</sup>, Hannah Groenen<sup>1</sup>, Christopher Faries<sup>1</sup>, Roderick S. Oosterwijk<sup>1</sup>, Esther M. van Leeuwen<sup>1</sup>, Francois Fay<sup>1,6</sup>, Elena Chepurko<sup>7</sup>, Thomas Reiner<sup>1,8</sup>, Raphael Duivenvoorden<sup>1,9</sup>, Lior Zangi<sup>7</sup>, Rick M. Dijkhuizen<sup>3</sup>, Sjoerd Hak<sup>5</sup>, Filip K. Swirski<sup>10,11</sup>, Matthias Nahrendorf<sup>10,11</sup>, Carlos Pérez-Medina<sup>1,12</sup>, Abraham J. P. Teunissen<sup>1</sup>, Zahi A. Fayad<sup>1</sup>, Claudia Calcagno<sup>1</sup>, Gustav J. Strijkers<sup>1,13</sup> and Willem J. M. Mulder<sup>1,2,14,15</sup> ✉

**Ischaemic heart disease evokes a complex immune response. However, tools to track the systemic behaviour and dynamics of leukocytes non-invasively in vivo are lacking. Here, we present a multimodal hot-spot imaging approach using an innovative high-density lipoprotein-derived nanotracer with a perfluoro-crown ether payload (<sup>19</sup>F-HDL) to allow myeloid cell tracking by <sup>19</sup>F magnetic resonance imaging. The <sup>19</sup>F-HDL nanotracer can additionally be labelled with zirconium-89 and fluorophores to detect myeloid cells by in vivo positron emission tomography imaging and optical modalities, respectively. Using our nanotracer in atherosclerotic mice with myocardial infarction, we observed rapid myeloid cell egress from the spleen and bone marrow by in vivo <sup>19</sup>F-HDL magnetic resonance imaging. Concurrently, using ex vivo techniques, we showed that circulating pro-inflammatory myeloid cells accumulated in atherosclerotic plaques and at the myocardial infarct site. Our multimodality imaging approach is a valuable addition to the immunology toolbox, enabling the study of complex myeloid cell behaviour dynamically.**

Unravelling the immune system's role in pathophysiological processes has not only deepened and broadened our understanding of disease but has also yielded new therapeutic avenues<sup>1</sup>. In this context, research that focuses on immune cell dynamics is becoming increasingly relevant<sup>2,3</sup>. A vast body of recent research has shown that atherosclerosis, the underlying cause of ischaemic heart disease, is a lipid-driven disease that is also largely dependent on immune cell influx<sup>4</sup>. Moreover, cardiovascular events themselves mobilize immune cells and accelerate ongoing atherosclerosis<sup>5</sup>. This contemporary, more complex view of ischaemic heart disease has resulted in the first clinical trial targeting inflammation with the goal of reducing the risk of recurrent cardiovascular events<sup>6</sup>.

Although many different aspects of myeloid cell dynamics in ischaemic heart disease have been decoded<sup>7</sup>, including their deployment from the bone marrow<sup>8</sup> and spleen<sup>9</sup>, current knowledge is exclusively based on snapshot immunological assays. Further, it is becoming more evident that these processes

interact systemically<sup>10–13</sup>. Without suitable in vivo read-outs, an all-encompassing view of these different processes is difficult to acquire. Therefore, this study's goal was to develop nanotechnology that can probe different aspects of myeloid cell dynamics in ischaemic heart disease using multimodal imaging. We developed and applied so-called high-density lipoprotein (HDL) nanotracers with a lipophilic perfluoro-crown ether (PFCE; <sup>19</sup>F-HDL) payload to enable hot-spot <sup>19</sup>F magnetic resonance imaging (MRI) (Fig. 1a). These <sup>19</sup>F-HDL nanotracers can be additionally labelled with zirconium-89 (<sup>89</sup>Zr) and/or fluorophores for in vivo detection by positron emission tomography (PET) imaging, a range of ex vivo nuclear methods and optical techniques, such as flow cytometry (Fig. 1a). In this study, using this <sup>19</sup>F-HDL-facilitated multimodal in vivo imaging approach, we studied myeloid cells in the bone marrow and spleen and monitored the migration of these cells and their accumulation in inflammatory tissues in mouse models of atherosclerosis and myocardial infarction (MI; Fig. 1b).

<sup>1</sup>BioMedical Engineering and Imaging Institute, Icahn School of Medicine at Mount Sinai, New York, NY, USA. <sup>2</sup>Department of Medical Biochemistry, Amsterdam University Medical Centers, University of Amsterdam, Amsterdam, the Netherlands. <sup>3</sup>Biomedical MR Imaging and Spectroscopy Group, Center for Image Sciences, University Medical Center Utrecht/Utrecht University, Utrecht, the Netherlands. <sup>4</sup>Instituto de Ciencias ICUAP, Benemérita Universidad Autónoma de Puebla, Puebla, Mexico. <sup>5</sup>Department of Circulation and Medical Imaging, Faculty of Medicine and Health Sciences, Norwegian University of Science and Technology, Trondheim, Norway. <sup>6</sup>Institut Galien Paris Sud, Faculté de Pharmacie, CNRS, Université Paris-Sud, Université Paris-Saclay, Paris, France. <sup>7</sup>Cardiovascular Research Center, Icahn School of Medicine at Mount Sinai, New York, NY, USA. <sup>8</sup>Department of Radiology, Memorial Sloan-Kettering Cancer Center and Weill Cornell Medical College, New York, NY, USA. <sup>9</sup>Department of Nephrology, Radboud Institute for Molecular Life Sciences, Radboud University Medical Center, Nijmegen, the Netherlands. <sup>10</sup>Center for Systems Biology, Massachusetts General Hospital, Harvard Medical School, Boston, MA, USA. <sup>11</sup>Department of Radiology, Massachusetts General Hospital, Harvard Medical School, Boston, MA, USA. <sup>12</sup>Centro Nacional de Investigaciones Cardiovasculares Carlos III, Madrid, Spain. <sup>13</sup>Department of Biomedical Engineering and Physics, Amsterdam University Medical Centers, University of Amsterdam, Amsterdam, the Netherlands. <sup>14</sup>Department of Oncological Sciences, Icahn School of Medicine at Mount Sinai, New York, NY, USA. <sup>15</sup>Laboratory of Chemical Biology, Department of Biomedical Engineering and Institute for Complex Molecular Systems, Eindhoven University of Technology, Eindhoven, the Netherlands. ✉e-mail: [willem.mulder@mssm.edu](mailto:willem.mulder@mssm.edu)

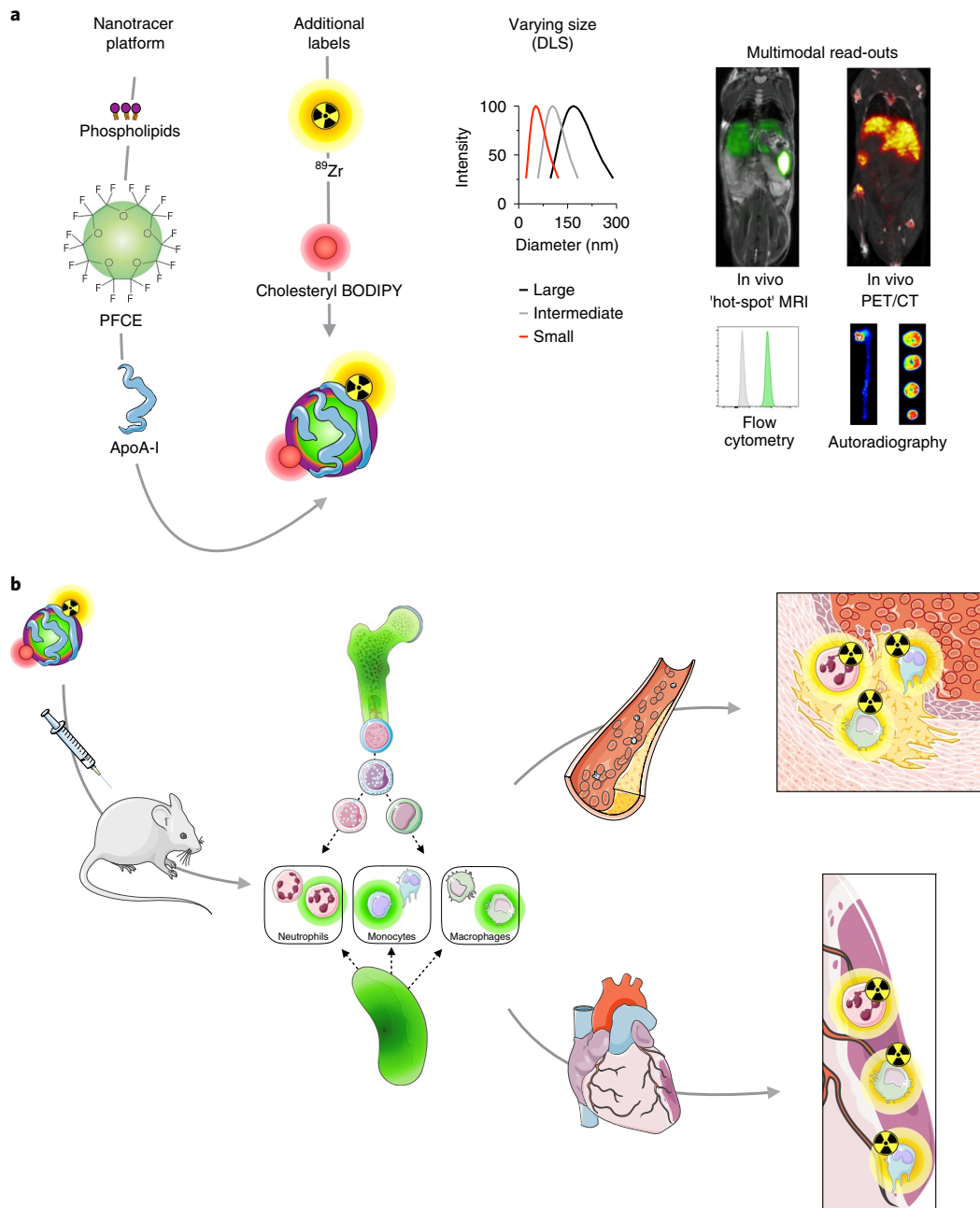


**Fig. 1 | Nanotracer platform with multimodal evaluation in ischaemic heart disease. a**, The nanotracer platform consists of a PFCE core surrounded by a phospholipid layer stabilized by ApoA-I. Additional labelling with  $^{89}\text{Zr}$  and cholesteryl BODIPY allows PET imaging and optical assays, respectively. We developed three  $^{19}\text{F}$ -HDL nanotracer formulations of varying sizes: small (approximately 40 nm); intermediate (approximately 105 nm); and large (approximately 180 nm). The lines represent their respective DLS-determined size distribution. **b**, Myeloid cell dynamics in the context of ischaemic heart disease. A mouse is injected with the nanotracer, which accumulates in the spleen and bone marrow as it is taken up by neutrophils, monocytes and macrophages. Egress from the spleen and bone marrow leads to subsequent nanotracer accumulation at the infarcted myocardium and atherosclerotic plaque. CT, computed tomography.

### Developing and characterizing multimodal nanotracers

We present a strategy to incorporate perfluorocarbons into high-density lipoprotein-like nanocarriers. Using this approach, we developed three formulations with varying  $^{19}\text{F}$  payloads and sizes. These three differently sized  $^{19}\text{F}$ -HDL nanotracers were composed of a perfluoro-crown ether core covered by a corona of phospholipids and apolipoprotein A-I (ApoA-I). Their hydrodynamic diameters were respectively 40 nm (small), 105 nm (intermediate) and 180 nm (large), as measured by dynamic light scattering (DLS); all remained stable at 37 °C in PBS for 10 d (Figs. 1a and 2a(i) and

Supplementary Fig. 1a). Transmission electron microscopy corroborated these DLS findings and showed a narrow size distribution of mostly spherical structures (Fig. 2a(ii)). In an ensuing *in vivo*  $^{19}\text{F}$  MRI study, the differently sized nanotracers were screened for their ability to accumulate in the spleen and bone marrow. Two days post-injection, mice were anaesthetized and underwent preclinical MRI using a dedicated  $^{19}\text{F}/^1\text{H}$  combination coil. Anatomical information was acquired using a standard  $^1\text{H}$  MRI protocol, while hot-spot  $^{19}\text{F}$  MRI was facilitated by a  $^{19}\text{F}$  three-dimensional fast low angle shot (FLASH) sequence to quantitatively visualize  $^{19}\text{F}$ -HDL nanotracers.

$^{19}\text{F}$  MRI revealed that the largest nanotracer displayed the most pronounced splenic uptake, while mice injected with the intermediate and small formulations showed splenic uptake levels comparable to those of the liver (Fig. 2a(iii)). Quantitative analyses of the spleen indicated a significantly higher target-to-background ratio (TBR) for the large nanotracer ( $24.4 \pm 7.3$ ) compared to the small and intermediate formulations ( $10.4 \pm 5.1$  and  $8.8 \pm 2.1$ , respectively;  $P < 0.01$ ; Fig. 2b). Moreover, the largest formulation also displayed the strongest bone marrow uptake in the spine, while liver and kidney uptake did not differ among the three formulations (Fig. 2b and Supplementary Fig. 1b). Lastly, absolute muscle uptake for all  $^{19}\text{F}$ -HDL formulations was similar, thereby justifying its use as the 'background' signal for TBR calculations (Supplementary Fig. 1c).

Encouraged by the pronounced spleen uptake, we selected the large nanotracer for the ensuing extensive *in vivo* characterization. In a separate group of mice, fluorescently labelled  $^{19}\text{F}$ -HDL was intravenously injected and allowed to distribute for 48 h, after which the animals were killed for flow cytometry experiments to study the cellular affinity of the largest nanotracer in the spleen and bone marrow. In the spleen, we observed significantly stronger uptake by myeloid cells—macrophages, neutrophils and monocytes—compared to lymphocytes; in the bone marrow, pro-inflammatory  $\text{Ly6C}^{\text{high}}$  monocytes took up most of  $^{19}\text{F}$ -HDL ( $P < 0.01$  and  $P = 0.005$ , respectively; Fig. 2c and Supplementary Fig. 2a,b). To study its *in vivo* behaviour quantitatively, we radiolabelled the  $^{19}\text{F}$ -HDL nanotracer with the long-lived (78.4 h) radioisotope  $^{89}\text{Zr}$  to enable PET imaging. In contrast to  $^{19}\text{F}$  MRI, this imaging method is highly sensitive, but we limited its use to 3 d due to the physical decay half-life of  $^{89}\text{Zr}$ . The core of the nanotracer cannot be radiolabelled because of the perfluoro-crown ether's physico-chemical properties and the  $^{19}\text{F}$ -HDL formulation procedure. Therefore, we performed three alternative  $^{89}\text{Zr}$  labelling strategies involving conjugating the chelator desferrioxamine B (DFO) with the nanotracer to allow complexation of  $^{89}\text{Zr}$ , thereby generating  $^{89}\text{Zr}$ - $^{19}\text{F}$ -HDL. Free  $^{89}\text{Zr}$  was removed by size-exclusion chromatography (Supplementary Fig. 1d). The three radiolabelling strategies, involving (1) DFO-functionalized ApoA-I, (2) DFO-functionalized phospholipid and (3) using a lipophilic version of DFO called DFO- $\text{C}_{34}$  showed similar PET imaging patterns, albeit clearance dynamics (Fig. 2d and Supplementary Fig. 1e,f) and reproducibility varied. These differences probably result from differences in *in vivo* remodelling kinetics. For example, phospholipids are known to exchange between lipoproteins avidly, while ApoA-I is more tightly bound and accumulates in the kidneys, hence the differences in blood half-life and kidney uptake<sup>14–16</sup>. These data underscore that ApoA-I labelling did not impact this protein's natural function.  $^{89}\text{Zr}$  labelling through  $\text{C}_{34}$ -DFO resulted in an imaging signature very similar to the  $^{19}\text{F}$  MRI results. *Ex vivo* gamma counting 2 d after  $^{89}\text{Zr}$ - $^{19}\text{F}$ -HDL injection validated the *in vivo* findings.

For the 180 nm  $^{89}\text{Zr}$ - $^{19}\text{F}$ -HDL, the spleen showed higher or similar uptake compared to the liver, irrespective of the  $^{89}\text{Zr}$  labelling strategy ( $P < 0.005$ ; Fig. 2d). PET imaging showed  $^{89}\text{Zr}$ - $^{19}\text{F}$ -HDL in the circulation 5 min post-injection (Fig. 2e, arrows) and mostly accumulated in the spleen, liver and kidneys 1 h post-injection (Fig. 2e). A PET scan 48 h post-injection corroborated the  $^{19}\text{F}$  MRI findings in Fig. 2a, displaying high uptake in the spleen with substantial uptake in the liver and accumulation in the bone marrow (Fig. 2e). We drew blood at multiple time points and calculated a circulation half-life of 6.2 h (Fig. 2f, with DFO-functionalized ApoA-I). It must be stressed that owing to the relatively rapid accumulation of the nanotracer in the spleen and bone marrow, the differences in remodelling kinetics had little impact on overall biodistribution. Subsequent experiments in *ApoE*<sup>-/-</sup> mice were performed with  $^{89}\text{Zr}$ - $^{19}\text{F}$ -HDL using labelling strategies (2) and (3).

The  $^{19}\text{F}$ -HDL nanotracer's *in vivo* resilience was studied longitudinally in wild-type mice (Fig. 2g). The  $^{19}\text{F}$  MRI signal remained stable over time in the bone marrow and spleen (Fig. 2h); flow cytometry quantification of fluorescently labelled nanotracers showed uptake by myeloid cells ( $\text{CD11b}^+$ ) (Supplementary Fig. 2c). Importantly, the noise and muscle quantified by  $^{19}\text{F}$  MRI did not differ over time (Supplementary Fig. 1g).

Based on its ability to track myeloid cells over prolonged periods of time *in vivo*, we next set out to employ the  $^{19}\text{F}$ -HDL nanotracer to study myeloid cell dynamics in ischaemic heart disease mouse models by multimodal imaging.

### Evaluation of myeloid cell dynamics in atherosclerosis development

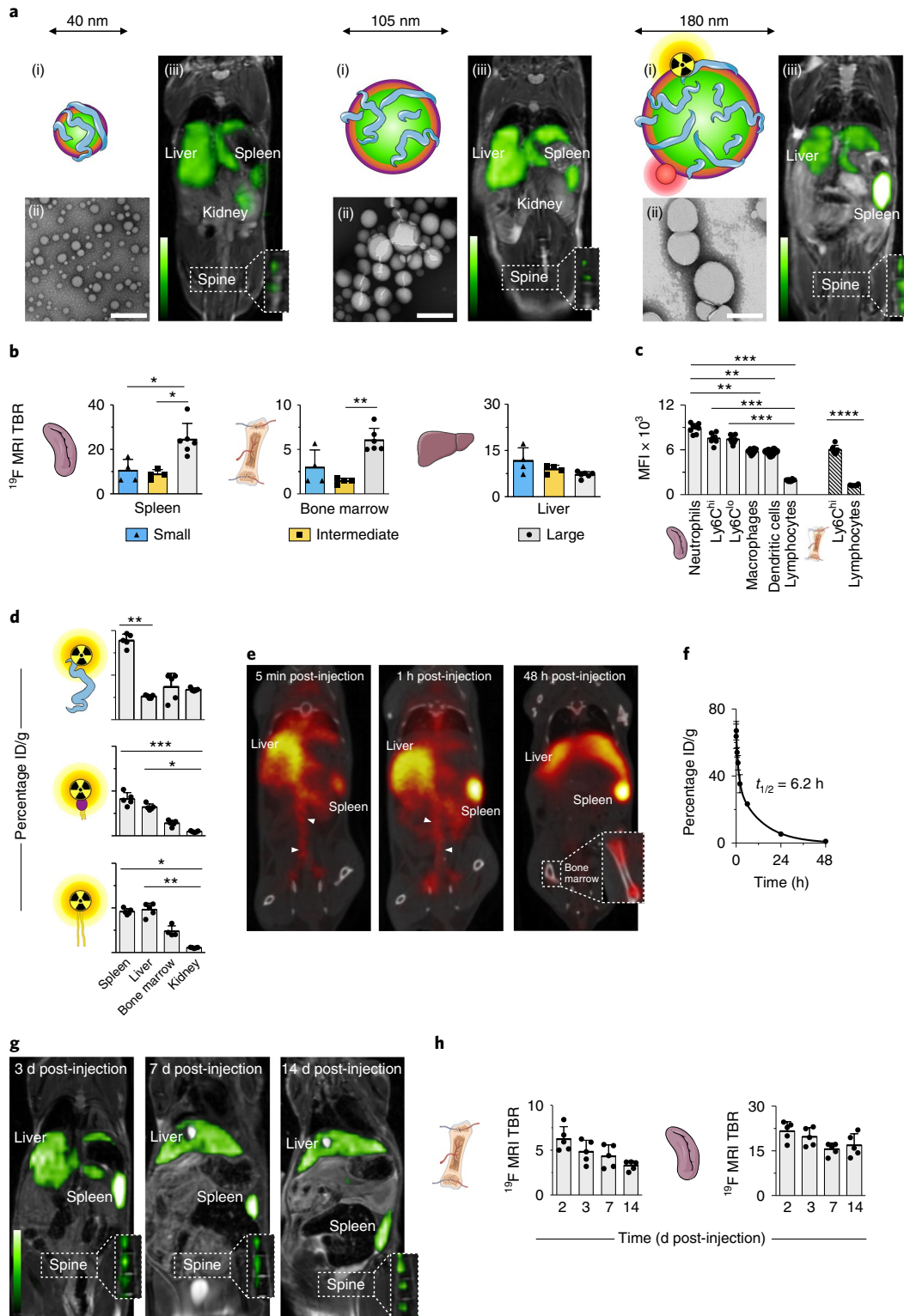
To study myeloid cell dynamics in the context of chronic inflammation, we used the well-established apolipoprotein E knockout (*ApoE*<sup>-/-</sup>) mouse model of atherosclerosis. In these animals, the ApoE ligand's absence in combination with a Western diet results in atherosclerotic lesions that progress over time<sup>17</sup>. We investigated myeloid cell dynamics in different atherosclerosis disease stages in *ApoE*<sup>-/-</sup> mice fed a Western diet for 0, 6 or 12 weeks, referred to as *ApoE*<sup>-/-</sup><sub>0WD</sub>, *ApoE*<sup>-/-</sup><sub>6WD</sub> and *ApoE*<sup>-/-</sup><sub>12WD</sub>. On  $^{19}\text{F}$ -HDL administration and in line with our findings in wild-type mice, we observed high accumulations in the spleen and liver at 3 and 14 d post-injection for all atherosclerotic mice by *in vivo*  $^{19}\text{F}$  MRI (Fig. 3a). In addition, the bone marrow signal in the spine was similar for all groups (Fig. 3a). To study the subsets of myeloid cells associated with our nanotracer at different stages of atherosclerosis development, cells were extracted from spleens collected after killing age- and diet-matched *ApoE*<sup>-/-</sup> mice (Fig. 3b). The nanotracer primarily labelled neutrophils, macrophages and  $\text{Ly6C}^{\text{high}}$  monocytes (Fig. 3b).

Subsequently, we performed quantification of the  $^{19}\text{F}$  MRI signal in the spleen, liver and bone marrow at different stages during

**Fig. 2 | Developing and characterizing multimodal nanotracers.** **a**, (i) Schematic overview of  $^{19}\text{F}$ -HDL's different sizes: small (approximately 40 nm, left); intermediate (approximately 105 nm, middle) and large (approximately 180 nm, right) particles. (ii) Transmission electron microscopy images showing the sizes and shapes of different nanotracers (scale bar, 200 nm). (iii) Representative fused  $^1\text{H}$  and  $^{19}\text{F}$  MRI images 48 h post-injection of the nanotracers. The MRI was repeated for  $n = 4$  (small, intermediate) and  $n = 6$  (large) biologically independent samples. **b**, Quantification of all three formulations in the spleen, bone marrow and liver expressed as TBR where muscle serves as the 'background' signal.  $n = 4$  mice (small, intermediate);  $n = 6$  mice (large). \* $P = 0.001$  (spleen), \*\* $P = 0.0023$  (bone marrow). **c**, MFI for different cells in the spleen (left) and bone marrow (right).  $n = 8$  mice (spleen);  $n = 6$  mice (bone marrow). \*\*\*\* $P < 0.0001$ , \*\*\* $P = 0.0002$ , \*\* $P < 0.01$ . **d**, Biodistribution 48 h after  $^{89}\text{Zr}$ - $^{19}\text{F}$ -HDL injection in healthy mice with three different labelling strategies: DFO conjugated with ApoA-I (top); DFO conjugated with liposomes (middle); or  $\text{C}_{34}$ -DFO incorporated in the liposome layer (bottom).  $n = 5$  mice per labelling strategy. \*\*\*\* $P = 0.0005$ , \*\* $P < 0.001$ , \* $P < 0.05$ . **e**, Representative fused PET/computed tomography (CT) images at 5 min, 1 h and 48 h after  $^{89}\text{Zr}$ - $^{19}\text{F}$ -HDL injection (DFO conjugated with ApoA-I), including a magnified femur showing bone marrow. Dynamic PET/CT was repeated for  $n = 4$  biologically independent samples. **f**, Pharmacokinetic curve of  $^{89}\text{Zr}$ - $^{19}\text{F}$ -HDL in healthy mice.  $n = 3$  independent samples for the first three time points;  $n = 5$  independent samples for later time points. **g**, Representative fused  $^1\text{H}/^{19}\text{F}$  MRI images used to longitudinally evaluate  $^{19}\text{F}$ -HDL 3, 7 and 14 d post-injection with magnified sections of the spine. The experiments were repeated twice independently with similar results;  $n = 6$  biologically independent samples for each repetition. **h**, Quantified  $^{19}\text{F}$ -HDL signal on different days post-injection using longitudinal  $^{19}\text{F}$  MRI in the bone marrow (left) and spleen (right), respectively.  $n = 5$  mice (1 mouse was excluded based on Grubbs' test for outliers). A one-way Kruskal-Wallis test with Dunn's test for multiple comparisons was used unless otherwise stated. **b,c,d,f**, Data are shown as the mean  $\pm$  s.d.

atherosclerosis development (Fig. 4a). Over 28 d, the  $^{19}\text{F}$  MRI signal in the spleen, liver, bone marrow and kidney (Fig. 4a and Supplementary Fig. 3a,b) remained stable for all groups, with one exception. The spleen and liver  $^{19}\text{F}$  MRI signal in  $Apoe^{-/-}_{6\text{WD}}$  mice dropped significantly at 28 d post-injection ( $P=0.03$ ; Fig. 4a). This decrease in signal was accompanied by increased  $\text{Ly6C}^{\text{high}}$  monocytes in the aortas of  $Apoe^{-/-}_{6\text{WD}}$  mice compared to  $Apoe^{-/-}_{0\text{WD}}$  mice ( $P=0.002$ ), while no difference was found with  $Apoe^{-/-}_{12\text{WD}}$  mice ( $P=0.06$ ; Fig. 4b and

Supplementary Fig. 3c). The  $^{19}\text{F}$  MRI-visualized decrease in  $^{19}\text{F}$  MRI signal in  $Apoe^{-/-}_{6\text{WD}}$  mice could be the result of increased  $\text{Ly6C}^{\text{high}}$  monocyte recruitment from the bone marrow and spleen to the plaque (Fig. 4b) that occurs in the intermediate stages of atherosclerosis development<sup>18</sup>. In the advanced plaques of  $Apoe^{-/-}_{12\text{WD}}$  mice, local proliferation dominates macrophage accumulation in the vessel wall<sup>19</sup>, which explains the increased myeloid cell numbers in the vessel wall in the absence of myeloid cell egress from the spleen.



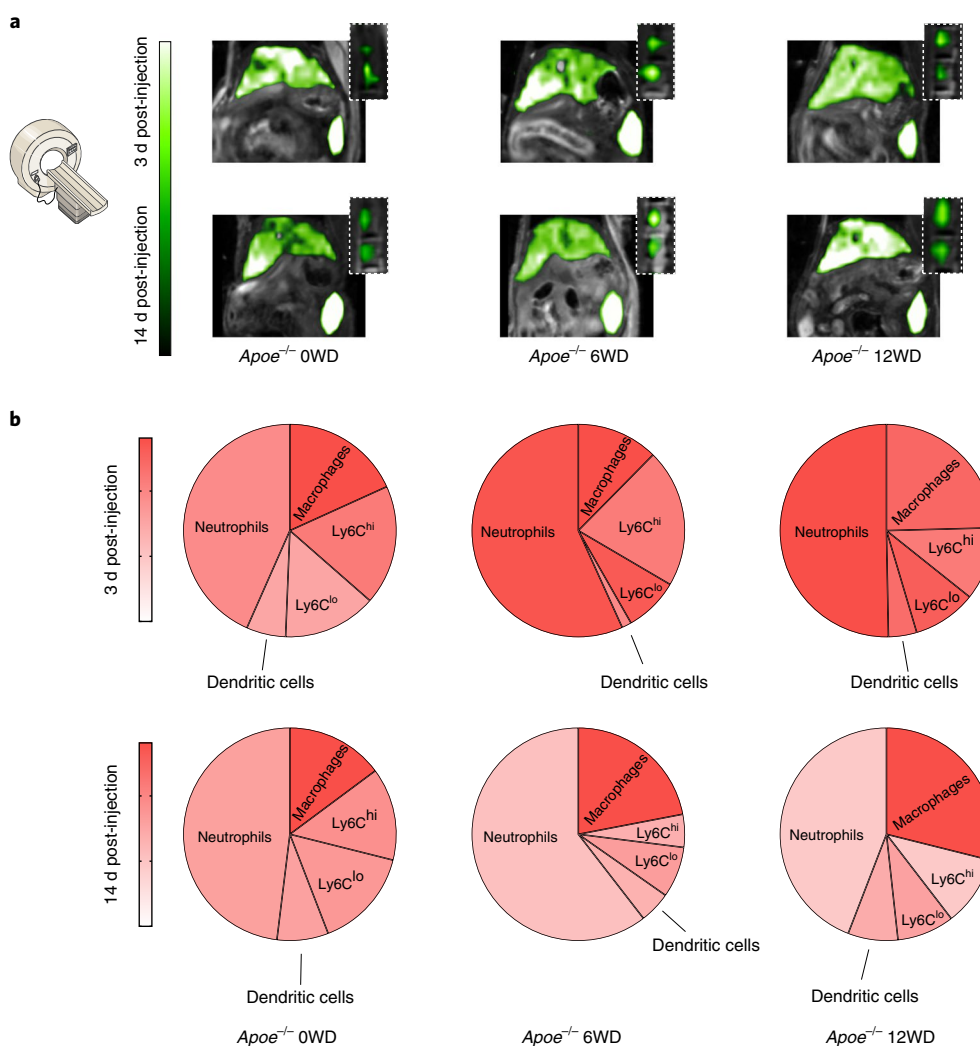


**Fig. 3 | Characterization in atherosclerosis.** **a**, Representative images of  $^1H/^{19}F$  MRI of upper abdominal area at 3 and 14 d post- $^{19}F$ -HDL injection with magnification of the spine containing bone marrow. Similar results were obtained in six ( $Apoe^{-/-}_{0WD}$ ,  $Apoe^{-/-}_{6WD}$ ) and five ( $Apoe^{-/-}_{12WD}$ ) independent experiments. **b**, MFI for different myeloid cell subsets in the spleen at 3 and 14 d after cholesteryl BODIPY- $^{19}F$ -HDL injection. The size of each wedge represents the relative contribution of each cell type to the total number of myeloid cells in the spleen.  $n=5$  for all groups  $Apoe^{-/-}_{0WD}$  and  $Apoe^{-/-}_{12WD}$  at 3 d;  $n=6$  for all groups  $Apoe^{-/-}_{6WD}$  and for  $Apoe^{-/-}_{12WD}$  at 14 d. Atherosclerotic  $Apoe^{-/-}$  mice had been fed a Western diet for 0 ( $Apoe^{-/-}_{0WD}$ ), 6 ( $Apoe^{-/-}_{6WD}$ ) or 12 ( $Apoe^{-/-}_{12WD}$ ) weeks at the time of injection.

In addition to identifying increased myeloid cell departure from the spleen in  $Apoe^{-/-}_{6WD}$  mice, this extensive longitudinal evaluation in mice with atherosclerosis also showed that the  $^{19}F$ -HDL nano-tracer was stable over time.

### Imaging of myeloid cell dynamics in MI

To study the effects of MI on myeloid cell dynamics in atherosclerosis, we fed  $Apoe^{-/-}$  mice a Western diet for 6 weeks and then subjected them to either permanent (MI<sup>+</sup>) or transient ligation of the left anterior descending artery, causing ischaemia–reperfusion injury (IRI)<sup>20,21</sup>. The latter is a relevant model of patients with MI in whom blockage of the coronary artery is treated, for example, by stenting<sup>22</sup>. Two days before inducing ischaemia,  $^{19}F$ -HDL was injected and allowed to accumulate in the spleen and bone marrow (see outline in Fig. 5a). We observed a rapid decline in  $^{19}F$  MRI TBR in the bone marrow and spleen 1 d after MI, for both permanent ligation and IRI, compared to non-MI controls (all  $P < 0.005$  except for bone marrow in IRI, where  $P < 0.02$ ; Fig. 5b,c). A similar decrease was observed for the liver but not the kidneys at 3 d ( $P < 0.005$ ; Fig. 5c and Supplementary Fig. 4a). Mice injected with

$^{89}Zr$ - $^{19}F$ -HDL and subjected to PET imaging 1 d after MI had a less pronounced haematopoietic organ signal decrease, while the liver signal did not differ among the groups, all based on gamma counting (Supplementary Fig. 4b,c). When  $^{19}F$  MR imaging was repeated 14 d post-injection, the differences between mice with MI (permanent ligation or IRI) and without MI persisted ( $P < 0.005$ ; Fig. 5d,e and Supplementary Fig. 4a). Other than tissues and organs directly involved in myeloid cell dynamics,  $^{89}Zr$ - $^{19}F$ -HDL distribution did not significantly differ between MI and non-MI  $Apoe^{-/-}$  mice (Supplementary Fig. 4d). The spleen acts as a reservoir that, in the event of MI or stroke, rapidly deploys large amounts of immune cells<sup>9</sup>. In addition, the liver and bone marrow serve as reservoirs for neutrophils released during acute injury<sup>23,24</sup>; these are phenomena that, thus far, have only been studied using *ex vivo* read-outs.

Pro-inflammatory cells deploying from the haematopoietic organs into the circulation can aggravate peripheral inflammation, for example, in atherosclerotic plaques<sup>5</sup>. In the current study, we observed decreased neutrophil levels in the bone marrow 1 d after permanent ligation; in the circulation, elevated levels of pro-inflammatory myeloid cells—neutrophils and  $Ly6C^{high}$



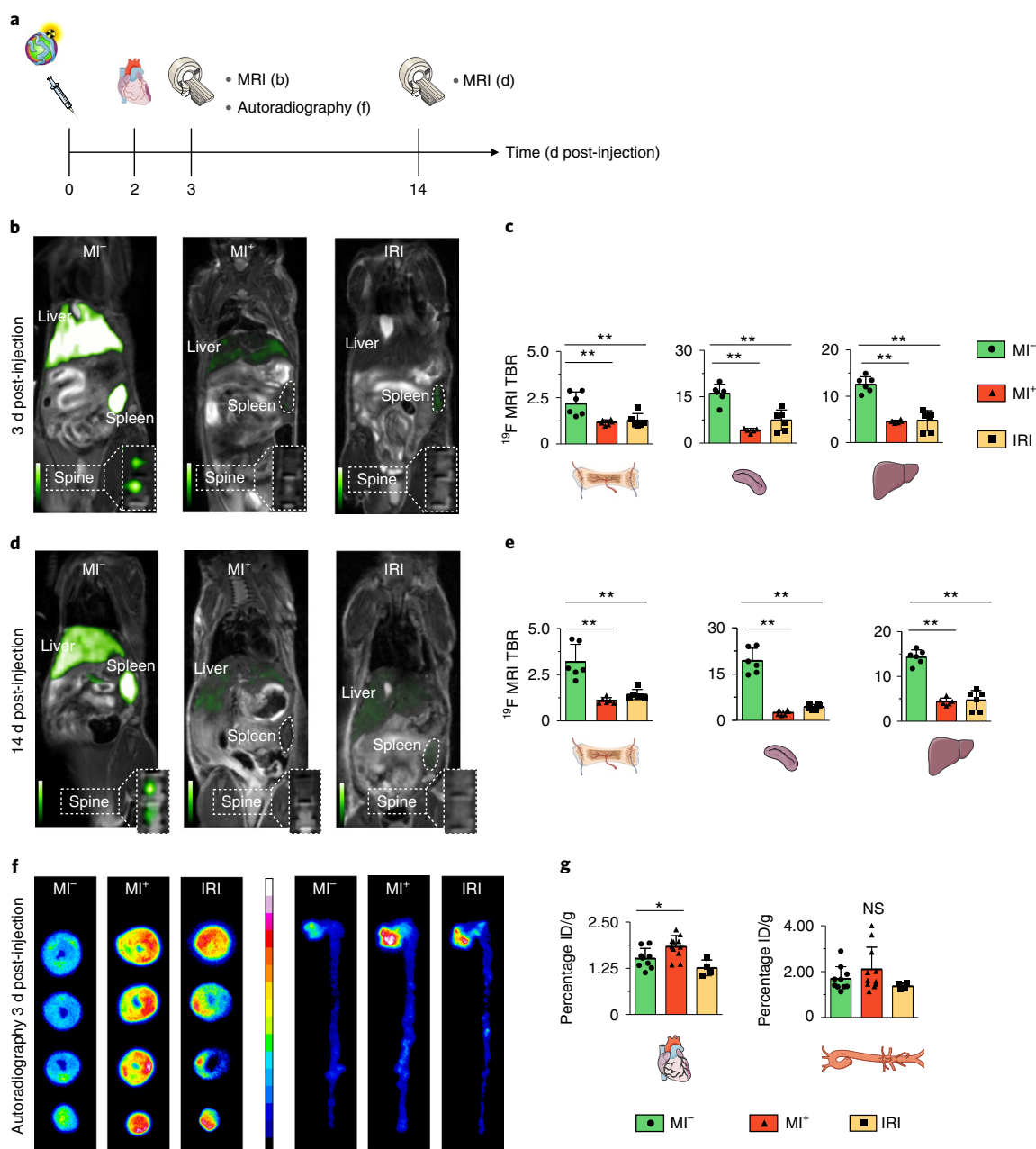


**Fig. 5 | Multimodal imaging of myeloid cell egress from haematopoietic organs and recruitment to inflammatory sites in MI.** **a**, Schematic overview of the experiments performed. MRI (**b**), MRI 3 d post injection as in **b**; Autoradiography (**f**), autoradiography 3 d post injection as in **f**; MRI (**d**), MRI 14 d post injection as in **d**. **b**, Representative  $^1\text{H}/^{19}\text{F}$  magnetic resonance images of  $\text{ApoE}^{-/-}$  mice without (left) and with permanent ( $\text{MI}^+$ , centre) or transient (IRI, right) MI 3 d post- $^{19}\text{F}$ -HDL injection. **c**, Quantification of  $^{19}\text{F}$ -HDL in the bone marrow, spleen and liver 3 d post- $^{19}\text{F}$ -HDL injection expressed as TBR where the muscle serves as the ‘background’ signal.  $n=6$  for MI, IRI and control groups except for  $\text{MI}^+$  spleen where  $n=5$ . One sample was excluded based on Grubbs’ test for outliers. A two-sided Mann-Whitney  $U$ -test was used for bone marrow (\*\* $P=0.0022$ ), spleen (\*\* $P=0.0043$ ) and liver (\*\* $P=0.0022$ ). **d**, Representative  $^1\text{H}/^{19}\text{F}$  MR images of  $\text{ApoE}^{-/-}$  mice without (left) and with permanent (centre) or transient (right) MI 14 days post- $^{19}\text{F}$ -HDL injection. **e**, Quantification of  $^{19}\text{F}$ -HDL in bone marrow, spleen and liver 14 d post-injection.  $n=6$  for all groups. A two-sided Mann-Whitney  $U$ -test was used for bone marrow (\*\* $P=0.0022$ ), spleen (\*\* $P=0.0022$ ) and liver (\*\* $P=0.0022$ ). **f**, Representative autoradiography of sliced heart sections and whole aortas from  $\text{ApoE}^{-/-}$  mice without MI (left) or 1 d after permanent (middle) or transient (right) MI 3 d after  $^{89}\text{Zr}$ - $^{19}\text{F}$ -HDL injection.  $n=7$  ( $\text{MI}^-$ );  $n=8$  ( $\text{MI}^+$ );  $n=4$  (IRI). **g**, Gamma counting quantification of whole hearts and aortas from  $\text{ApoE}^{-/-}$  mice without MI (green) or 1 d after permanent (red) or transient (yellow) MI and 3 d post- $^{89}\text{Zr}$ - $^{19}\text{F}$ -HDL injection.  $n=9$  for  $\text{MI}^-$ ,  $n=11$  for  $\text{MI}^+$  and  $n=4$  for IRI groups. A two-sided Mann-Whitney  $U$ -test was used. \* $P=0.0276$   $\text{MI}^+$  heart percentage ID/g compared to  $\text{MI}^-$ ;  $P=0.3418$  for  $\text{MI}^+$  aorta percentage ID/g compared to  $\text{MI}^-$ . **b, d**, Experiments were repeated in  $n=6$  mice per group with similar results. All data are shown as the mean  $\pm$  s.d.  $\text{ApoE}^{-/-}$  mice without MI are shown in green; mice with MI are shown in red (permanent ligation) and yellow (transient ligation). NS, not significant.

time, flow cytometry identified larger myeloid cell populations in the blood, the infarcted myocardium and the aorta. These increases coincided with enhanced myeloid cell accumulation as observed by ex vivo nuclear techniques. The apparent signal decline by  $^{19}\text{F}$  MRI

from the liver because of MI was an unexpected finding and warrants further research.

We developed a nanotracer-based multimodal imaging approach to study immune cell dynamics longitudinally at a systemic level.

In the current study, we used this imaging approach alongside cell-sorting techniques to unravel regulatory pathways and pathophysiological processes in cardiovascular disease. Implementation of our approach in clinical systems will potentially allow the study of immune cell dynamics in large animal models, an important—and required—intermediate step for clinical translation. Ultimately, we anticipate its use in other inflammatory diseases and to aid in the development and evaluation of immunotherapies.

### Online content

Any methods, additional references, Nature Research reporting summaries, source data, extended data, supplementary information, acknowledgements, peer review information; details of author contributions and competing interests; and statements of data and code availability are available at <https://doi.org/10.1038/s41565-020-0642-4>.

Received: 13 December 2018; Accepted: 16 January 2020;

Published online: 20 April 2020

### References

- Moore, K. J. & Tabas, I. Macrophages in the pathogenesis of atherosclerosis. *Cell* **145**, 341–355 (2011).
- Yona, S. et al. Fate mapping reveals origins and dynamics of monocytes and tissue macrophages under homeostasis. *Immunity* **38**, 79–91 (2013).
- Geissmann, F. et al. Development of monocytes, macrophages, and dendritic cells. *Science* **327**, 656–661 (2010).
- Swirski, F. K. & Nahrendorf, M. Leukocyte behavior in atherosclerosis, myocardial infarction, and heart failure. *Science* **339**, 161–166 (2013).
- Dutta, P. et al. Myocardial infarction accelerates atherosclerosis. *Nature* **487**, 325–329 (2012).
- Ridker, P. M. et al. Antiinflammatory therapy with canakinumab for atherosclerotic disease. *N. Engl. J. Med.* **377**, 1119–1131 (2017).
- Nahrendorf, M. Myeloid cell contributions to cardiovascular health and disease. *Nat. Med.* **24**, 711–720 (2018).
- Herisson, F. et al. Direct vascular channels connect skull bone marrow and the brain surface enabling myeloid cell migration. *Nat. Neurosci.* **21**, 1209–1217 (2018).
- Swirski, F. K. et al. Identification of splenic reservoir monocytes and their deployment to inflammatory sites. *Science* **325**, 612–616 (2009).
- Tawakol, A. et al. Relation between resting amygdalar activity and cardiovascular events: a longitudinal and cohort study. *Lancet* **389**, 834–845 (2017).
- Thackeray, J. T. et al. Myocardial inflammation predicts remodeling and neuroinflammation after myocardial infarction. *J. Am. Coll. Cardiol.* **71**, 263–275 (2018).
- Heidt, T. et al. Chronic variable stress activates hematopoietic stem cells. *Nat. Med.* **20**, 754–758 (2014).
- Roth, S. et al. Brain-released alarmins and stress response synergize in accelerating atherosclerosis progression after stroke. *Sci. Transl. Med.* **10**, ea01313 (2018).
- Pérez-Medina, C. et al. A modular labeling strategy for in vivo PET and near-infrared fluorescence imaging of nanoparticle tumor targeting. *J. Nucl. Med.* **55**, 1706–1711 (2014).
- Tang, J. et al. Immune cell screening of a nanoparticle library improves atherosclerosis therapy. *Proc. Natl Acad. Sci. USA* **113**, E6731–E6740 (2016).
- Pérez-Medina, C. et al. In vivo PET imaging of HDL in multiple atherosclerosis models. *JACC Cardiovasc. Imaging* **9**, 950–961 (2016).
- Nakashima, Y., Plump, A. S., Raines, E. W., Breslow, J. L. & Ross, R. ApoE-deficient mice develop lesions of all phases of atherosclerosis throughout the arterial tree. *Arterioscler. Thromb.* **14**, 133–140 (1994).
- Swirski, F. K. et al. Ly-6C<sup>hi</sup> monocytes dominate hypercholesterolemia-associated monocytosis and give rise to macrophages in atheromata. *J. Clin. Invest.* **117**, 195–205 (2007).
- Robbins, C. S. et al. Local proliferation dominates lesional macrophage accumulation in atherosclerosis. *Nat. Med.* **19**, 1166–1172 (2013).
- Panizzi, P. et al. Impaired infarct healing in atherosclerotic mice with Ly-6C<sup>hi</sup> monocytosis. *J. Am. Coll. Cardiol.* **55**, 1629–1638 (2010).
- von Elverfeldt, D. et al. Dual-contrast molecular imaging allows noninvasive characterization of myocardial ischemia/reperfusion injury after coronary vessel occlusion in mice by magnetic resonance imaging. *Circulation* **130**, 676–687 (2014).
- Heusch, G. et al. Cardiovascular remodelling in coronary artery disease and heart failure. *Lancet* **383**, 1933–1943 (2014).
- Kolaczowska, E. & Kubes, P. Neutrophil recruitment and function in health and inflammation. *Nat. Rev. Immunol.* **13**, 159–175 (2013).
- Soehnlein, O. Multiple roles for neutrophils in atherosclerosis. *Circ. Res.* **110**, 875–888 (2012).

**Publisher's note** Springer Nature remains neutral with regard to jurisdictional claims in published maps and institutional affiliations.

© The Author(s), under exclusive licence to Springer Nature Limited 2020

## Methods

**Formulating PFCE-loaded  $^{19}\text{F}$ -HDL nanotracers.** 1,2-Dimyristoyl-*sn*-glycero-3-phosphocholine (59 mg) and 1-myristoyl-2-hydroxy-*sn*-glycero-3-phosphocholine (41 mg), both obtained from Avanti Polar Lipids, were dissolved in 2 ml of chloroform. The chloroform solution was slowly dripped in hot PBS (10 ml, 80 °C). The obtained solution was stirred for 5 min at this temperature and then allowed to cool to room temperature. If necessary, additional PBS was added to obtain a total volume of 10 ml. The lipid solution (0.5 ml), PBS (4.5 ml) and PFCE (Oakwood Chemicals)—20  $\mu\text{l}$  for approximately 36 nm particles, 80  $\mu\text{l}$  for 105 nm particles and 160  $\mu\text{l}$  for 180 nm particles—were sonicated for 30 min at 0 °C using a 150 V/T ultrasonic homogenizer working at 30% power output for tip sonication. ApoA-I (0.5 mg), purified in house from human HDL, was added and the mixture was incubated at room temperature for at least 12 h, after which the mixture was shaken and left to stand for 30 s. Any precipitate formed was discarded and the remaining solution was transferred to a Vivaspin tube (Sartorius Stedim Biotech; 100 kDa molecular weight cut-off (MWCO) for approximately 36 and 105 nm sized particles, 1 MDa MWCO for approximately 180 nm particles). The tube was spun at 4,000g at 4 °C until the solution was concentrated to approximately 0.5 ml; then, the particles were resuspended by repeatedly moving them up and down a pipette. To determine particle size, an aliquot (10  $\mu\text{l}$ ) of the final particle solution was diluted in PBS (1 ml) and analysed by DLS to determine the mean number of the average size distribution. DLS measurements were performed on a NanoBrook ZetaPlus electrophoresis system (Brookhaven Instruments). The mean of the number distribution was taken as the particle size. All chemicals were obtained from Sigma-Aldrich unless otherwise stated.

### Determining PFCE concentration by $^{19}\text{F}$ nuclear magnetic resonance (NMR).

To determine the PFCE concentration in the prepared nanotracers, we prepared a solution containing nanotracers (90 vol%), deuterium oxide (10 vol%) and a known amount of sodium trifluoroacetate. We analysed the solution by  $^{19}\text{F}$  NMR and determined the PFCE concentration using sodium trifluoroacetate as the internal standard. We analysed the  $^{19}\text{F}$  NMR samples using a Bruker 600 Ultrashield magnet connected to a Bruker Avance 600 console. Data were processed using Topspin v.3.5p17.

**Modifying  $^{19}\text{F}$ -HDL nanotracers with cholesteryl BODIPY.** Cholesteryl 4,4-difluoro-5,7-dimethyl-4-bora-3a,4a-diaza-*s*-indacene-3-dodecanoate (cholesteryl BODIPY) was obtained from Thermo Fisher Scientific (catalogue no. C3927MP). To prepare the nanotracers containing the cholesteryl BODIPY dye, we used the same protocol as for the unlabelled particles, except that cholesteryl BODIPY was added to the lipid mixture at 1.0 wt% of the amount of lipids used.

**Functionalizing nanotracers with DFO for radiolabelling.** Three strategies were pursued, either involving the DFO labelling of ApoA-I (strategy 1) or incorporating a DSPE-DFO or aliphatic  $\text{C}_{34}$ -DFO conjugate (strategies 2 and 3, respectively). While all labelling strategies resulted in stable  $^{89}\text{Zr}$ -labelled nanotracers, we found that  $\text{C}_{34}$ -DFO-based labelling (strategy 3) is the most reproducible.

Strategy 1 involved DFO labelling of ApoA-I in preformulated nanotracers. DFO was conjugated to ApoA-I by basifying pre-made nanotracers in approximately 1–3 ml of PBS using a carbonate buffer (1 M, pH 9) until a pH of approximately 8.5 was reached. The ApoA-I concentration was kept between 1 and 10  $\text{mg ml}^{-1}$  (assuming all ApoA-I used in formulating the nanotracers was recovered). *p*-NCS-Bz-DFO (Macrocylics) was dissolved in dimethylsulfoxide (DMSO) to obtain 5  $\text{mg ml}^{-1}$  solution and added to the nanotracers until a twofold molar excess of *p*-NCS-Bz-DFO (753  $\text{g mol}^{-1}$ ) over ApoA-I (28,000  $\text{g mol}^{-1}$ ) was achieved. To minimize the influence of DMSO on the nanotracers, the *p*-NCS-Bz-DFO solution was added in aliquots of 5  $\mu\text{l}$  and the total DMSO concentration was kept below 5 vol%. The solution containing nanotracers and *p*-NCS-Bz-DFO was incubated at 37 °C in a water bath for 2 h and subsequently transferred to a Vivaspin centrifugal filtration tube (100 kDa MWCO). The Vivaspin tube was spun at 4,000g and 4 °C until a volume of 1–2 ml was obtained; PBS (2 ml) was added and the solution was again concentrated to a volume of 1–2 ml. This washing step was repeated twice, after which particles were resuspended by repeatedly moving them up and down a pipette.

Strategies 2 and 3 involved incorporating DSPE-DFO or  $\text{C}_{34}$ -DFO into the nanotracers. To prepare nanotracers containing DSPE-DFO or  $\text{C}_{34}$ -DFO, we used the same protocol as for formulating the unlabelled nanotracers, except that either DSPE-DFO or  $\text{C}_{34}$ -DFO (synthesized using procedures previously reported by us)<sup>14,15</sup> was added to the lipid mixture at 0.5 wt% of the amount of lipids used.

**Radiolabelling DFO-bearing nanotracers with  $^{89}\text{Zr}$ .**  $^{89}\text{Zr}$  oxalate was made at the Memorial Sloan Kettering Cancer Center using an EBCO TR19/9 variable-beam energy cyclotron via the  $^{89}\text{Y}(p,n)^{89}\text{Zr}$  reaction and purified using a method published previously<sup>23</sup>, resulting in a  $^{89}\text{Zr}$  solution in 1 M aqueous oxalic acid. The  $^{89}\text{Zr}$  solution was diluted with PBS and aqueous sodium sulfate solution (1 M) added until a pH of 6.8–7.4 was reached. This solution was added to a solution of DFO-functionalized nanotracers (containing either DSPE-DFO,  $\text{C}_{34}$ -DFO or ApoA-I-DFO); the obtained solution (1–2 ml total) was incubated for 1 h in a thermoshaker at 37 °C. The Zr-labelled nanotracers were purified using

a PD-10 column (Sephadex G-25 M; GE Healthcare Life Sciences) using PBS as the eluent. In the DSPE-DFO- or  $\text{C}_{34}$ -DFO-labelled nanotracers (strategy 2 or 3), nanoparticles were washed 3 times with PBS by centrifugal filtration using a 10 kDa MWCO Vivaspin tube. Radiochemical purity was assessed using size-exclusion chromatography and radio-high-performance liquid chromatography; typically, a purity >95% was achieved. Radiochemical yields were typically between 50 and 90% for strategy 1, and reproducibly >80% for strategies 2 and 3. Size-exclusion chromatography and radio-high-performance liquid chromatography analyses were performed on a Shimadzu system equipped with a Superdex 10/300 SEC column using a flow rate of 1  $\text{ml min}^{-1}$  and demineralized water as the eluent. A Scan-RAM radiodetector (Lablogic) was used.

**Animals.** All animal experiments were performed in accordance with protocols approved by the Institutional Animal Care and Use Committee of the Icahn School of Medicine at Mount Sinai and followed the National Institutes of Health guidelines for animal welfare.

**Mouse models.** Eight-week-old female *Apoe*<sup>-/-</sup> (B6.129P2-*Apoe*<sup>tm1Unc/J</sup>) mice were purchased from The Jackson Laboratory and fed a cholesterol-enriched Western diet (Harlan Teklad TD.88137, 42% of calories from fat) for either 0, 6 or 12 weeks before injection and remained on this diet for the rest of the experiment. Due to the elevated circulating low-density lipoprotein concentrations resulting from their lack of APOE protein, these animals develop atherosclerotic plaques, especially at locations with disturbed flow, that is, the aortic root and the aortic arch with its branches<sup>17,26</sup>. Age-matched female C57BL/6J mice received regular chow and served as controls.

**MI.** Age-matched, 8-week-old female *Apoe*<sup>-/-</sup> mice received a Western diet for 6 weeks before undergoing permanent or temporary ligation of the left descending artery to induce MI, as described in full detail by Tarnavski et al.<sup>27</sup>. Anaesthesia was induced using ketamine (100  $\text{mg kg}^{-1}$ ) with xylazine (10  $\text{mg kg}^{-1}$ ) intraperitoneally and maintained using isoflurane. Analgesia was provided using buprenorphine (0.1  $\text{mg kg}^{-1}$ ) before and 12 h after surgery. The left side of thorax was shaved and disinfected, a thoracotomy was performed using the fifth or fourth intercostal space and a retractor was used to keep the surgical field exposed. Attention was paid not to puncture the left lung. Temporary ligation was maintained for 40 min by a small tube between the ligation suture and left anterior descending artery. All infarctions were created 2 d post-injection with either  $^{19}\text{F}$ -HDL or  $^{89}\text{Zr}$ - $^{19}\text{F}$ -HDL. For more details, see the outline in Fig. 5a.

**MRI.** C57BL/6J or *Apoe*<sup>-/-</sup> mice were injected with 1.3  $\mu\text{l}$  of  $^{19}\text{F}$ -HDL solution per gram of body weight via the lateral tail vein. Mice were anesthetized with an isoflurane (Baxter Healthcare)/oxygen gas mixture (2% for induction, 1% for maintenance) and images were acquired on a BioSpec 70/30 7t scanner (Bruker) using a  $^{19}\text{F}/^1\text{H}$  birdcage coil for mice (MR Coils B.V.). After acquiring localizer scans, a hydrogen ( $^1\text{H}$ ) three-dimensional FLASH sequence was performed to identify the liver and spleen (orientation, coronal; repetition time, 20 ms; echo time, 3.7 ms; field of view, 60  $\times$  60  $\times$  30  $\text{mm}^3$ ; matrix, 256  $\times$  128  $\times$  128; reconstructed voxel size, 0.23  $\times$  0.23  $\times$  0.23  $\text{mm}^3$ ; flip angle, 20°; signal averages, 2; acquisition time, 6 min 8 s). An additional  $^1\text{H}$  turbo rapid imaging with refocused echoes, T2-weighted sequence was also acquired for this purpose (orientation, coronal; repetition time, 3,000 ms; echo time, 33 ms; number of slices, 27; slice thickness, 1 mm; slice gap, 0.1 mm; field of view, 60  $\times$  30  $\text{mm}^2$ ; matrix size, 256  $\times$  128; rapid imaging with refocused echoes, factor 8; pixel size 0.23  $\times$  0.23  $\text{mm}^2$ ; signal averages, 12; acquisition time, 9 min 36 s). Next, the coil was switched to  $^{19}\text{F}$  mode. After centring the frequency on the PFCE peak, a three-dimensional FLASH sequence was performed to quantify the  $^{19}\text{F}$  signal in the liver and spleen (orientation, coronal; repetition time, 20 ms; echo time, 2.9 ms; field of view, 60  $\times$  60  $\times$  30  $\text{mm}^3$ ; matrix, 64  $\times$  32  $\times$  32; voxel size, 0.94  $\times$  0.94  $\times$  0.94  $\text{mm}^3$ ; flip angle, 25°; signal averages, 200; acquisition time, 1 h 8 min 16 s).

**PET/CT imaging.** C57BL/6J or *Apoe*<sup>-/-</sup> mice were injected with the  $^{89}\text{Zr}$ - $^{19}\text{F}$ -HDL (0.07–0.30 mCi) in 100  $\mu\text{l}$  PBS solution via the lateral tail vein. Animals were anaesthetized with an isoflurane/oxygen gas mixture (2% for induction, 1% for maintenance) and a scan was performed using a nanoScan PET/CT (Mediso). Wild-type mice were imaged immediately after injection followed by a second imaging 48 h later. *Apoe*<sup>-/-</sup> mice were imaged 72 h post-injection. A whole-body CT scan was performed (energy 50 kVp; current 180  $\mu\text{A}$ s; isotropic voxel size, 0.25  $\times$  0.25  $\text{mm}^2$ ) followed by a 20- or 60-min PET scan. Reconstruction for the PET data used the CT acquisition for attenuation correction. Reconstruction was performed using the TeraTomo three-dimensional reconstruction algorithm using Mediso Nucline Nanoscan v 3.00.020.0000. Coincidences were filtered with an energy window between 400 and 600 keV. Voxel size was isotropic, with a 0.6 mm width, and reconstruction was applied for two full iterations, with 6 subsets per iteration.

**Image analysis.** All imaging data obtained were analysed using OsiriX v.5.6 software (OsiriX Foundation). Regions of interest (ROIs) were measured by manually drawing a contour on different tissues. In the case of  $^{19}\text{F}$  MRI, a TBR was calculated by dividing the mean of multiple (>10) maximum ROI values ( $\text{ROI}_{\text{max}}$ ) from the tissue of interest by the mean of multiple  $\text{ROI}_{\text{max}}$  from muscle tissue.

**Pharmacokinetics and biodistribution in mice.** The blood radioactivity half-life was determined by serial blood draws from the tail vein at 1, 5, 30, 60 and 120 min and 6, 24 and 48 h after  $^{89}\text{Zr}$ - $^{19}\text{F}$ -HDL injection. Blood was weighed and counted using a Wizard<sup>26</sup> 2480 Automatic Gamma Counter (PerkinElmer). After the scans were completed, animals were killed and perfused; tissues (brain, heart, lungs, aorta, spleen, liver, kidneys, skeletal muscle and bone marrow) were collected, blotted and weighed in pre-weighed tubes. Radioactivity content was measured by gamma counting and tissue radioactivity concentration was calculated and expressed as the percentage of the injected dose per gram of tissue (ID/g) or normalized by the activity found in muscle tissue.

**autoradiography.** Digital autoradiography was performed to determine  $^{89}\text{Zr}$  distribution within the whole aorta and infarct. Samples were placed in a film cassette against a phosphorimaging plate (BASMS-2325; Fujifilm) for 1.5 h (whole aortas) or 2 h (hearts) and stored at  $-20^{\circ}\text{C}$ . Phosphorimaging plates were read at a pixel resolution of 25  $\mu\text{m}$  with a Typhoon 7000IP plate reader (GE Healthcare). Quantification was carried out with ImageJ software (version 1.49, 2015).

**Flow cytometry.** For flow cytometry analysis, blood was obtained by cardiac puncture and collected in an EDTA-coated tube. Mice were subsequently perfused through the left ventricle with 10 ml cold PBS. Femur and spleen were collected. The aorta, from the aortic root to the iliac bifurcation, was collected. The infarcted heart tissue was collected and weighed. The aorta was minced and digested using an enzymatic digestion solution containing liberase TH (4 U ml<sup>-1</sup>; Roche), DNase I (40 U ml<sup>-1</sup>; Sigma-Aldrich) and hyaluronidase (60 U ml<sup>-1</sup>; Sigma-Aldrich) in PBS. Heart tissue was minced and digested using an enzymatic digestion solution containing DNase I (60 U ml<sup>-1</sup>), collagenase type I (450 U ml<sup>-1</sup>), collagenase type XI (125 U ml<sup>-1</sup>) and hyaluronidase (60 U ml<sup>-1</sup>; all Sigma-Aldrich) in PBS. Aortas and heart tissues were incubated for 1 h at 37  $^{\circ}\text{C}$  under agitation. Cells were filtered through a 70  $\mu\text{m}$  cell strainer and washed with fluorescence-activated cell-sorting (FACS) buffer (Dulbecco's PBS with 1% FCS, 0.5% BSA, 0.1% NaN<sub>3</sub> and 1 mM EDTA). Blood was incubated with lysis buffer for 4 min and washed with FACS buffer; this was repeated twice more. Spleens were weighed. A 25 mg piece was mashed, filtered through a 70  $\mu\text{m}$  cell strainer, incubated with lysis buffer for 4 min and washed with FACS buffer. Bone marrow was flushed out of the femur with PBS, filtered through a 70  $\mu\text{m}$  cell strainer, incubated with lysis buffer for 30 s and washed with FACS buffer. Single-cell suspensions were stained with the following monoclonal antibodies: PE anti-mouse/human CD11b (clone M1/70; BioLegend; 1:200); PE anti-mouse F4/80 (clone BM8; BioLegend; 1:100); FITC anti-mouse CD11c (clone N418; BioLegend; 1:200); purified anti-mouse CD45 (clone 30-F11; BioLegend; 1:200); APC rat anti-mouse Ly6C (clone AL-21; BD Biosciences; 1:200); and a lineage cocktail (Lin) containing APC anti-mouse CD90.2 (Thy-1.2) (clone 53-2.1; eBioscience; 1:200), PE anti-mouse TER-119 (clone TER-119; eBioscience; 1:200), purified anti-mouse NK-1.1 (clone PK136; eBioscience; 1:200), PE anti-mouse CD49b (pan-NK cells) (clone DX5; eBioscience; 1:200), purified anti-mouse/human CD45R/B220 (clone RA3-6B2; eBioscience; 1:200), purified anti-mouse CD103 (clone 2E7; eBioscience; 1:200) and purified anti-mouse Ly-6G (clone 1A8; eBioscience; 1:100). Macrophages were identified as CD45<sup>+</sup>, CD11b<sup>high</sup>, Lin<sup>-low</sup>, CD11c<sup>low</sup> and F4/80<sup>hi</sup>. Monocytes were identified as CD45<sup>+</sup>, CD11b<sup>high</sup>, Lin<sup>-low</sup>, CD11c<sup>low</sup> and Ly6C<sup>high/low</sup>. Neutrophils were identified as CD45<sup>+</sup>, CD11b<sup>high</sup> and Lin<sup>+</sup>. Lymphocytes were identified as CD45<sup>+</sup> and Lin<sup>+</sup>. CD11b<sup>+</sup> cells were identified as CD45<sup>+</sup> and CD11b<sup>+</sup>. To measure the cellular specificity of 19F-HDL, cholesteryl BODIPY- $^{19}\text{F}$ -HDL was intravenously injected 48 h before euthanasia. Cholesteryl BODIPY uptake was measured in the fluorescein isothiocyanate channel. Mean fluorescence intensity (MFI) was corrected to fluorescent bead signal (SPHERO AccuCount Fluorescent Particles; Spherotech). Data were acquired on a Fortessa flow cytometer (BD Biosciences) and were analysed using FlowJo v.10.4.0 (FlowJo LLC).

**Statistics.** Data are presented as the mean  $\pm$  s.d. Differences were evaluated using a two-sided Mann-Whitney *U*-test (between two groups) or a Student's *t*-test for

repeated measures (between two groups). For differences between more than two groups, a Kruskal-Wallis test was followed by Dunn's test for multiple comparisons unless otherwise stated. For all tests,  $P < 0.05$  represents statistical significance. Statistical analyses were performed with Prism v.6.0c (GraphPad Software).

**Reporting Summary.** Further information on research design is available in the Nature Research Reporting Summary linked to this article.

### Data availability

The data that support the plots within this paper and other findings of this study are available from the corresponding author upon reasonable request.

### References

- Holland, J. P., Sheh, Y. & Lewis, J. S. Standardized methods for the production of high specific-activity zirconium-89. *Nucl. Med. Biol.* **36**, 729–739 (2009).
- Plump, A. S. et al. Severe hypercholesterolemia and atherosclerosis in apolipoprotein E-deficient mice created by homologous recombination in ES cells. *Cell* **71**, 343–353 (1992).
- Tarnavski, O. et al. Mouse cardiac surgery: comprehensive techniques for the generation of mouse models of human diseases and their application for genomic studies. *Physiol. Genomics* **16**, 349–360 (2004).

### Acknowledgements

This work was supported by De Drie Lichten Foundation in the Netherlands (M.L.S.); American Heart Association grant nos. 17PRE33660729 (M.L.S.) and 16SDG3139000 (C.P.M.); German Research Foundation grant nos. MA 7059/1 (A.M.) and HO 5953/1-1 (M.N.); National Heart, Lung, and Blood Institute grant nos. HL096576, HL117829, HL139598 and HL128264; the MGH Research Scholar Award (M.N. and F.K.S.); Dutch Applied and Engineering Sciences (TTW) grant no. 14716 (G.J.S.); National Institutes of Health (NIH) grants: R01HL143814, R01HL144072, R01HL135878 and P01HL131478 (Z.A.F.); R01HL144072, R01CA220234 and P01HL131478 (W.J.M.M.); and the Netherlands Organisation for Scientific Research (NWO) grants: Vidi 91713324 and Vici 91818622 (W.J.M.M.).

### Author contributions

M.L.S. coordinated the experimental planning and execution. W.J.M.M. conceptualized and designed the study. A.J.P.T., B.L.S.-G., C.P.-M. and E.D.K. developed, synthesized, characterized and labelled the nanotracers. M.L.S., A.E.M., M.M.T.L., J.C.V., Y.C.T., A.M., E.D.K., N.A.T.S., A.M.S., H.G., C.F., R.S.O., E.M.L., F.F. and E.C. conducted the in vivo experiments. C.C., Z.A.F. and G.J.S. developed the imaging protocols. M.N. and F.K.S. developed the flow cytometry protocols and provided immunological insights. R.M.D., R.D. and L.Z. contributed expertise on cardiovascular disease mouse models. S.H. and T.R. designed nanotracer labelling strategies. M.L.S. and W.J.M.M. wrote the manuscript and M.L.S. produced the figures for initial submission. All authors reviewed and edited the manuscript before submission.

### Competing interests

The authors declare no competing interests.

### Additional information

**Supplementary information** is available for this paper at <https://doi.org/10.1038/s41565-020-0642-4>.

**Correspondence and requests for materials** should be addressed to W.J.M.M.

**Peer review information** *Nature Nanotechnology* thanks Jeff Bulte, Christian Schulz and the other, anonymous, reviewer(s) for their contribution to the peer review of this work.

**Reprints and permissions information** is available at [www.nature.com/reprints](http://www.nature.com/reprints).

## Reporting Summary

Nature Research wishes to improve the reproducibility of the work that we publish. This form provides structure for consistency and transparency in reporting. For further information on Nature Research policies, see [Authors & Referees](#) and the [Editorial Policy Checklist](#).

### Statistics

For all statistical analyses, confirm that the following items are present in the figure legend, table legend, main text, or Methods section.

n/a Confirmed

- |                                     |                                     |  |
|-------------------------------------|-------------------------------------|--|
| <input type="checkbox"/>            | <input checked="" type="checkbox"/> | The exact sample size ( $n$ ) for each experimental group/condition, given as a discrete number and unit of measurement  |
| <input type="checkbox"/>            | <input checked="" type="checkbox"/> | A statement on whether measurements were taken from distinct samples or whether the same sample was measured repeatedly  |
| <input type="checkbox"/>            | <input checked="" type="checkbox"/> | The statistical test(s) used AND whether they are one- or two-sided<br><i>Only common tests should be described solely by name; describe more complex techniques in the Methods section.</i>   |
| <input checked="" type="checkbox"/> | <input type="checkbox"/>            | A description of all covariates tested   |
| <input type="checkbox"/>            | <input checked="" type="checkbox"/> | A description of any assumptions or corrections, such as tests of normality and adjustment for multiple comparisons  |
| <input type="checkbox"/>            | <input checked="" type="checkbox"/> | A full description of the statistical parameters including central tendency (e.g. means) or other basic estimates (e.g. regression coefficient) AND variation (e.g. standard deviation) or associated estimates of uncertainty (e.g. confidence intervals) |
| <input type="checkbox"/>            | <input checked="" type="checkbox"/> | For null hypothesis testing, the test statistic (e.g. $F$ , $t$ , $r$ ) with confidence intervals, effect sizes, degrees of freedom and $P$ value noted<br><i>Give <math>P</math> values as exact values whenever suitable.</i>                            |
| <input checked="" type="checkbox"/> | <input type="checkbox"/>            | For Bayesian analysis, information on the choice of priors and Markov chain Monte Carlo settings   |
| <input checked="" type="checkbox"/> | <input type="checkbox"/>            | For hierarchical and complex designs, identification of the appropriate level for tests and full reporting of outcomes   |
| <input checked="" type="checkbox"/> | <input type="checkbox"/>            | Estimates of effect sizes (e.g. Cohen's $d$ , Pearson's $r$ ), indicating how they were calculated   |

*Our web collection on [statistics for biologists](#) contains articles on many of the points above.*

### Software and code

Policy information about [availability of computer code](#)

Data collection

Data analysis

For manuscripts utilizing custom algorithms or software that are central to the research but not yet described in published literature, software must be made available to editors/reviewers. We strongly encourage code deposition in a community repository (e.g. GitHub). See the Nature Research [guidelines for submitting code & software](#) for further information.

### Data

Policy information about [availability of data](#)

All manuscripts must include a [data availability statement](#). This statement should provide the following information, where applicable:

- Accession codes, unique identifiers, or web links for publicly available datasets
- A list of figures that have associated raw data
- A description of any restrictions on data availability

## Field-specific reporting

Please select the one below that is the best fit for your research. If you are not sure, read the appropriate sections before making your selection.

- Life sciences       Behavioural & social sciences       Ecological, evolutionary & environmental sciences

## Life sciences study design

All studies must disclose on these points even when the disclosure is negative.

Sample size	Sample size was determined based on the amplitude differences observed during the development of the 19F-HDL nanobiologic (Fig. 1b). We calculated that at least 5 mice per group were needed to provide a statistical power of 80% to detect a difference between the groups, assuming a two-sided alpha of 0.05.
Data exclusions	Pre-established exclusion criteria were defined as outliers detected in Grubbs' test (Alpha = 0.05).
Replication	19F MRI was repeated for the large formulations in wild type mice to verify the initial results. Gamma counting of radioactive samples was repeated to verify results. All attempts of replication were successful.
Randomization	Animals were allocated to different experimental designs on the basis of randomly chosen cage numbers.
Blinding	Data analysis and acquisition were performed by different individuals without knowledge of group allocation.

## Reporting for specific materials, systems and methods

We require information from authors about some types of materials, experimental systems and methods used in many studies. Here, indicate whether each material, system or method listed is relevant to your study. If you are not sure if a list item applies to your research, read the appropriate section before selecting a response.

### Materials & experimental systems

n/a	Involved in the study
<input type="checkbox"/>	<input checked="" type="checkbox"/> Antibodies
<input checked="" type="checkbox"/>	<input type="checkbox"/> Eukaryotic cell lines
<input checked="" type="checkbox"/>	<input type="checkbox"/> Palaeontology
<input type="checkbox"/>	<input checked="" type="checkbox"/> Animals and other organisms
<input checked="" type="checkbox"/>	<input type="checkbox"/> Human research participants
<input checked="" type="checkbox"/>	<input type="checkbox"/> Clinical data

### Methods

n/a	Involved in the study
<input checked="" type="checkbox"/>	<input type="checkbox"/> ChIP-seq
<input type="checkbox"/>	<input checked="" type="checkbox"/> Flow cytometry
<input checked="" type="checkbox"/>	<input type="checkbox"/> MRI-based neuroimaging

## Antibodies

Antibodies used	anti-CD11b (clone M1/70, BioLegend, 101228, 1:200), anti-F4/80 (clone BM8, BioLegend, 123114, 1:100); anti-CD11c (clone N418, BioLegend, 117310, 1:200), anti-CD45 (clone 30-F11, BioLegend, 103138, 1:200), anti-Ly6C (clone AL-21, BD Biosciences, 560592, 1:200), anti-CD90.2 (clone 53-2.1, eBioscience, 48-0902-821, 1:200), anti-Ter119 (clone TER119, eBioscience, 48-5921-82, 1:200), anti-NK1.1 (clone PK136, eBioscience, 48-5941-82, 1:200), anti-CD49b (clone DX5, eBioscience, 48-5971-82, 1:200), anti-CD45R/B220 (clone RA3-6B2, eBioscience, 48-0452-82, 1:200), anti-CD103 (clone 2E7, eBioscience, 48-1031-82, 1:200) and anti-Ly6G (clone 1A8, eBioscience, 48-9668-82, 1:100).
Validation	According to statements on the manufacturers websites, each antibody used in this study was validated for flow cytometry applications. As stated on manufacturers/suppliers websites, the following primary antibodies have been validated for reactivity in mouse: anti-CD11b, anti-F4/80, anti-CD11c, anti-CD45, anti-Ly6C, anti-CD90.2, anti-Ter119, anti-NK1.1, anti-CD49b, anti-CD103, anti-Ly6G. As stated on manufacturers/suppliers websites, the following antibodies have been validated for reactivity in mouse and human: anti-CD45R/B220.

## Animals and other organisms

Policy information about [studies involving animals](#); [ARRIVE guidelines](#) recommended for reporting animal research

Laboratory animals	ApoE <sup>-/-</sup> mice (B6.129P2-Apoetm1Unc/J) and wild type mice (C57BL/6J) all female and 8 weeks old.
Wild animals	The study did not involve wild animals.
Field-collected samples	The study did not involve samples collected from the field.
Ethics oversight	All animal experiments were performed in accordance with protocols approved by the Institutional Animal Care and Use Committees of the Icahn School of Medicine at Mount Sinai and followed National Institutes of Health guidelines for animal welfare.

Note that full information on the approval of the study protocol must also be provided in the manuscript.

## Flow Cytometry

### Plots

Confirm that:

- The axis labels state the marker and fluorochrome used (e.g. CD4-FITC).
- The axis scales are clearly visible. Include numbers along axes only for bottom left plot of group (a 'group' is an analysis of identical markers).
- All plots are contour plots with outliers or pseudocolor plots.
- A numerical value for number of cells or percentage (with statistics) is provided.

### Methodology

Sample preparation

Flow cytometry analyses were done on cells from C57BL/6 and Apoe<sup>-/-</sup> mice. Blood was obtained by cardiac puncture and collected in an EDTA-coated tube. Mice were subsequently perfused through the left ventricle with 10 mL cold PBS. Femur and spleen were harvested. The aorta, from aortic root to the iliac bifurcation, was collected. The infarcted heart tissue was collected and weighed. The aorta was minced and digested using an enzymatic digestion solution containing liberase TH (4 U/mL) (Roche), deoxyribonuclease (DNase) I (40 U/mL) (Sigma-Aldrich), and hyaluronidase (60 U/mL) (Sigma-Aldrich) in PBS. Heart tissue was minced and digested using an enzymatic digestion solution containing DNase (60 U/mL), collagenase I (450 U/mL), collagenase XI (125 U/mL), hyaluronidase (60 U/mL) (all Sigma-Aldrich) in PBS. Aortas and heart tissues were incubated for 1 hour at 37°C under agitation. Cells were filtered through a 70 µm cell strainer and washed with FACS buffer (DPBS with 1% FBS, 0.5% BSA, 0.1% Na<sub>3</sub> and 1mM EDTA). Blood was incubated with lysis buffer for 4 minutes and washed with FACS buffer. Spleens were weighed. A piece of 25 mg was mashed, filtered through a 70 µm cell strainer, incubated with lysis buffer for 4 minutes and washed with FACS buffer. Bone marrow was flushed out of the femur with PBS, filtered through a 70 µm cell strainer, incubated with lysis buffer for 30 seconds and washed with FACS buffer.

Instrument

Data were acquired on a LSRFortessa (BD Bioscience)

Software

Data were analyzed using FlowJo v10.4.0 (Tree Star).

Cell population abundance

Cells were not sorted for this study.

Gating strategy

For all experiments, preliminary FSC/SSC gates were used to exclude debris. Subsequently, FSC-A/FSC-H gates were used to select singlets. In the following plots DAPI-, and CD45+ cells were selected. Examples of the subsequent plots are all shown in the manuscript and/or supplementary material. Macrophages were identified as CD45+, CD11bhigh, Lin-/low, CD11clow and F4/80hi. Monocytes were identified as CD45+, CD11bhigh, Lin-/low, CD11clow and Ly6Chigh/low. Neutrophils were identified as CD45+, CD11bhigh and Lin+. Lymphocytes were identified as CD45+ and Lin+. CD11b+ cells were identified as CD45+ and CD11b+.

- Tick this box to confirm that a figure exemplifying the gating strategy is provided in the Supplementary Information.